chemistry

MDPI

Article

Structure, Stability, and Initial Transformation of Clusters $(NiO_2)_n$: A DFT Study Targeting Oxygen-Rich Intermediates in Nit-Kel-Oxygen Systems

Joaquín Hernández-Fernández [1,2,*], Rafael González-Cuello [3] and Rodrigo Ortega-Toro [3]

[1] Chemistry Program, Department of Natural and Exact Sciences, University of Cartagena, San Pablo Campus, Cartagena de Indias 130015, Colombia
[2] Department of Natural and Exact Sciences, Universidad de la Costa, Barranquilla 080002, Colombia
[3] Food Packaging and Shelf-Life Research Group (FP&SL), Food Engineering Program, University of Cartagena, Cartagena de Indias 130015, Colombia; rgonzalezc1@unicartagena.edu.co (R.G.-C.)
* Correspondence: jhernandezf@unicartagena.edu.co

Abstract

The structure, relative stability, spin-state preference, and preliminary oxygen-release behavior of small nickel–oxygen clusters, $(NiO_2)_n$ (n = 1–4), were investigated using density functional theory at the M06-2X/def2-TZVP level of theory. Several initial topologies and spin multiplicities were explored to distinguish between dissociated Ni···O_2 solutions, bonded dioxo-like arrangements, and side-on metal–dioxygen motifs. For the monomer, the lowest-energy solution of the fully explored set corresponds to a non-bonded Ni···O_2 arrangement; however, when the analysis is restricted to chemically bonded NiO_2 minima, the linear high-spin O–Ni–O structure is the most stable configuration. The side-on η^2-O_2 motif was found as a higher-energy bonded minimum, retaining an elongated O–O bond and therefore representing an activated dioxygen-like species. ELF and LOL analyses were used as complementary localization descriptors to distinguish between the electronically separated oxo-like domains of the linear structure and the more coupled localization pattern of the side-on dioxygen adduct. Aggregation from n = 2 to n = 4 suggests a transition from compact bridged motifs to more open Ni–O frameworks. However, the size-dependent trend is discussed only within the explicitly explored conformational space. Preliminary analysis of O_2 release from the tetramer indicates that oxygen evolution is not a simple dissociation event but involves substantial structural reorganization. Overall, the results support the view that small $(NiO_2)_n$ clusters may behave as metastable oxygen-rich intermediates, while also highlighting the strong sensitivity of their energetic ordering to spin state, topology, and structural relaxation.

Keywords: nickel–oxygen clusters; density functional theory; spin multiplicity; oxygen-rich intermediates; dioxo-like species; metal–dioxygen motifs; O_2 release

Check for updates

Academic Editor: Ryohei Kishi

Received: 8 May 2026
Revised: 10 June 2026
Accepted: 11 June 2026
Published: 23 June 2026

Copyright: © 2026 by the authors. Licensee MDPI, Basel, Switzerland. This article is an open access article distributed under the terms and conditions of the Creative Commons Attribution (CC BY) license.

1. Introduction

Rechargeable metal–oxygen systems have gained relevance due to their high theoretical energy density and the physicochemical complexity of oxygen reduction and evolution [1–3]. In this type of platform, the nature of oxygen-rich intermediates controls not only the overall reaction pathway but also the product morphology, transformation kinetics, charge mobility, and electrochemical reversibility of the system [4–6]. Consequently, elucidating the structural and electronic properties of metal–dioxygen species at molecular

and subnanometric scales is a central problem in computational chemistry applied to electroactive materials [7–9]. Although isolated $(NiO_2)_n$ clusters should not be interpreted as directly deployable materials, their characterization can provide molecular-scale models of oxygen-rich intermediates relevant to rechargeable metal–oxygen batteries, oxygen-evolution processes, and the rational design of nickel–oxygen electroactive materials [1–9]. Within this context, the Ni–O system is particularly attractive due to the electronic flexibility of nickel, its ability to stabilize various oxidation states, and the possibility of generating interactions of different character with oxygenated fragments [10–12]. However, NiO_2 stoichiometry alone does not allow us to directly infer whether the corresponding species should be described as an adduct with a retained O_2 motif, a peroxo form, a superoxo-like entity, or a structure closer to a dioxo motif [13–15]. This structural and electronic ambiguity becomes even more important when considering small aggregates, where cooperation between units can induce O–O bond rearrangements, spin redistribution, and drastic changes in the relative stability of isomers [16–18].

From a mechanistic perspective, the characterization of $(NiO_2)_n$ clusters is relevant because such species could act as transient reservoirs of activated oxygen, precursors of early aggregation, or intermediates in O_2 evolution and structural rearrangement pathways [19–21]. Therefore, the problem should not be restricted to identifying a single stable geometry but should systematically explore alternative topologies, different spin multiplicities, and possible transformation trajectories [7,13,16]. A study of this nature allows us to establish whether the system retains a chemically recognizable O–O fragment when interacting with nickel, whether aggregation becomes thermodynamically favorable with cluster size, and whether oxygen release constitutes a spontaneous pathway or requires substantial prior reorganization [8,14,20]. Based on these considerations, the objective of the present work was to analyze the structural, energetic, electronic, and spin-state landscape of small $(NiO_2)_n$ clusters with n = 1–4 using density functional theory. The study was designed to address four specific questions: whether the NiO_2 monomer preferentially exists as a bonded dioxo-like structure, a metal–dioxygen adduct, or a dissociated Ni···O_2 arrangement; how the preferred topology changes upon aggregation; how spin multiplicity affects the relative stability of the optimized structures; and whether oxygen release from larger clusters proceeds through direct dissociation or through prior structural reorganization. Because the study is restricted to a finite set of initial topologies and multiplicities, the conclusions are formulated in terms of the explored conformational and spin-state space rather than as an exhaustive global optimization of all possible $(NiO_2)_n$ clusters [9,15,18–21].

2. Materials and Methods

2.1. Overall Study Design

The computational study was organized into three sequential stages. First, the NiO_2 monomer was examined using several chemically distinct initial geometries and spin multiplicities to distinguish bonded dioxo-like structures, side-on/end-on dioxygen adducts, and dissociated Ni···O_2 solutions. Second, small aggregates $(NiO_2)_n$ with n = 2–4 were constructed from different initial topologies to evaluate how aggregation affects the preferred geometry, spin state, and Ni–O connectivity. Third, a preliminary O_2-release pathway was explored from the selected tetrameric structure to determine whether oxygen evolution proceeds through direct dissociation or through prior reorganization of the Ni–O framework. The study was not intended to optimize all possible isomers; therefore, all structural conclusions are limited to the topologies and multiplicities explicitly considered.

2.2. Construction of Initial Structures

Initial structures were generated to cover chemically distinct bonding motifs rather than to optimize a single predefined arrangement. For NiO_2, four starting families were considered: linear dioxo O–Ni–O, angular dioxo O–Ni–O, end-on η^1-O_2, and side-on η^2-O_2. For the aggregates, initial geometries were built by combining NiO_2 units into open, bridged, compact, non-planar, semi-cyclic, and curved arrangements, depending on cluster size. During optimization, all structures were allowed to relax without imposing symmetry constraints, so that changes in connectivity, O–O retention or cleavage, and Ni–O bridge formation could emerge from the calculation [22,23].

The complete list of initial topologies, final optimized structures, spin multiplicities, relative Gibbs free energies, and vibrational validation results is provided in the Supporting Information (Table S1). In the main text, only the lowest-energy vibrationally stable structures and chemically relevant alternatives are discussed to avoid overemphasizing duplicated, unstable, or non-bonded solutions (Table 1).

Table 1. Summary of the initial structural families, spin multiplicities, and vibrational validation criteria considered for the conformational exploration of $(NiO_2)_n$ clusters.

System	Initial Structural Families	Multiplicities Considered	Validation Criterion
NiO_2	Linear, angular, end-on η^1-O_2, side-on η^2-O_2	1, 3, 5	$N_{imag} = 0$ for minima
$(NiO_2)_2$	Open, compact, non-planar, semi-cyclic	1, 3, 5	$N_{imag} = 0$ for minima
$(NiO_2)_3$	Bridged open, compact, non-planar, semi-cyclic curved	3, 5, 7	$N_{imag} = 0$ for minima
$(NiO_2)_4$	Open curved, pointed open	7	$N_{imag} = 0$ for minima

From the optimized monomers, aggregates $(NiO_2)_n$ were constructed, initially for n = 2–4, by manual combination of NiO_2 units in open, cyclical, almost planar, and compact non-planar arrays. In each case, at least in the initial geometry, the local identity of the NiO_2 units was preserved, allowing the system to relax fully during optimization. This procedure aligns with recent computational strategies employed in the study of subnanometer clusters and metal nanoaggregates, in which exploring multiple initial topologies is necessary to avoid artificial local minima and more reliably capture structural evolution with size [24–27].

2.3. Level of Theory, Geometric Optimization, and Vibrational Validation

All calculations were performed with Gaussian 16 B.01 using the M06-2X functional and the def2-TZVP basis set. M06-2X was selected because it is a hybrid meta-GGA functional commonly used for main-group thermochemistry, noncovalent interactions, and reaction energetics. At the same time, def2-TZVP provides a balanced triple-ζ description suitable for transition-metal–oxygen clusters at moderate computational cost [28,29]. Nevertheless, nickel–oxygen species may exhibit pronounced spin-state sensitivity and possible multiconfigurational character. The present energetic ordering should therefore be interpreted as a comparative analysis within the M06-2X/def2-TZVP framework rather than as a definitive high-level benchmark. Scalar-relativistic corrections, spin–orbit coupling effects, and additional multireference calculations were not explicitly included. Their possible influence is expected to be most relevant when comparing electronic states separated by small energy differences. Accordingly, the discussion emphasizes robust structural trends and avoids assigning absolute energetic certainty to closely spaced spin states [28–30].

Vibrational validation was performed using harmonic frequency calculations. Structures were accepted as true minima only when they did not present imaginary frequen-

cies [31]. In the cases intended to explore reaction routes, the transition states were identified by the presence of a single imaginary frequency associated with the vibrational mode of the reactive coordinate [31,32].

2.4. Exploring Spin States

For each structural family, several spin multiplicities were evaluated because the relative stability of nickel–oxygen clusters cannot be assigned a priori. For the monomer, the singlet, triplet, and quintet states were considered. For larger aggregates, the multiplicity range was expanded according to the number of nickel centers and the expected possibility of ferro- or antiferromagnetic coupling between local spin centers. Final spin-state assignments were based on Gibbs free energies of vibrationally stable optimized structures, together with the final $\langle S^2 \rangle$ values. Structures with imaginary frequencies were not considered true minima and were excluded from the final stability hierarchy. If two calculations converged to the same geometry, energy, and spin expectation value, they were treated as duplicate solutions rather than independent states [33,34].

The dimer was evaluated in the singlet, triplet, and quintet states. Higher-spin states were not included in the present dataset and are therefore acknowledged as a limitation of the current spin-state sampling.

The evaluated spin multiplicities also provide a qualitative basis for discussing the expected magnetic behavior of the optimized clusters. Structures with multiplicity greater than one possess a non-zero total spin and are therefore expected to display open-shell paramagnetic behavior in the isolated-cluster description. In contrast, conventional closed-shell singlet solutions are nominally diamagnetic. Broken-symmetry singlet solutions may instead reflect antiferromagnetic coupling between local spin centers. However, a quantitative assignment of ferro- or antiferromagnetic coupling would require a dedicated analysis of local spin densities and exchange-coupling constants. The present interpretation is therefore restricted to the magnetic behavior inferred from the calculated total-spin multiplicities.

2.5. Thermodynamic Analysis and Stability Criteria

The relative stability of isomers with equal composition was evaluated using the Gibbs free energies obtained from frequency calculations [35]. For each stoichiometric set, the relative energies were defined with respect to the most stable minimum of the corresponding set. In addition, the aggregation trend was estimated using aggregation-free energies calculated from the global reaction $nNiO_2 \rightarrow (NiO_2)_n$ [36].

The thermodynamic discussion focused on the relative free energy of each isomer, the free energy of aggregation of each cluster, and, when relevant, the free energy of reaction for the transformation processes analyzed, since this approach allows comparison of alternative topologies and assessment of the stabilizing effect of aggregate growth [35,36].

The thermochemical quantities were obtained from harmonic-frequency calculations using the standard ideal-gas rigid-rotor harmonic-oscillator approximation. The calculated Gibbs free energies include translational, rotational, vibrational, and electronic contributions as implemented in Gaussian. Alternative spin multiplicities were evaluated through independent geometry optimizations and frequency calculations rather than through an explicit multistate electronic partition function. Thermally accessible excited electronic states were not incorporated explicitly.

No quasi-rigid-rotor harmonic-oscillator correction was applied to the low-frequency vibrational modes. Therefore, the reported Gibbs free energies should be interpreted as RRHO-based estimates. Because soft vibrational modes may affect the entropic contribution of flexible cluster structures, the thermodynamic discussion is restricted primarily to relative

trends within the explicitly explored set of structures. This limitation is particularly relevant for structures separated by small Gibbs free-energy differences.

2.6. Complementary Electronic Characterization Using Multiwfn

To delve deeper into the nature of the O–O bond and Ni–O interactions in monomers, the wave function files were exported in formatted format (.fchk) and analyzed with the Multiwfn 3.8 program. From these files, the electron localization (ELF) and orbital locator (LOL) functions were calculated to examine the spatial distribution of electron density and to evaluate the degree of electron localization in the system's binding regions [37,38].

2.7. Mechanistic Exploration of O_2 Evolution and Structural Reorganization

The O_2-release pathway was explored by optimizing the stationary points associated with the initial tetrameric reactant, a transition-state candidate, a reorganized intermediate, and the final product containing detached molecular oxygen. Harmonic frequency calculations at the same level of theory characterized each stationary point. Minima were accepted only when no imaginary frequencies were present, whereas transition-state candidates were accepted only when one imaginary frequency was found, and the associated normal mode corresponded to the expected O–O formation/cleavage or O_2-detachment coordinate. Relative free energies were calculated with respect to the selected tetrameric reactant. Because the pathway was constructed from selected stationary points, it should be interpreted as a preliminary mechanistic profile rather than a complete search for the reaction path [39].

3. Results and Discussion

3.1. Relative Stability and Structural Reorganization of NiO_2-Bonded Monomers

The conformational and spin-state exploration of NiO_2 revealed two energetic regimes that must be distinguished. When all optimized solutions within the sampled structural space are considered, the lowest Gibbs free energies correspond to non-bonded Ni···O_2 arrangements obtained from the end-on and side-on initial geometries in the triplet state. These structures do not preserve a chemically bonded NiO_2 framework and are therefore more appropriately described as dissociated or weakly interacting Ni + O_2 solutions rather than as genuine bonded NiO_2 minima. They were retained in the complete dataset to document the behavior of the explored potential-energy surface, but they were excluded from the energetic hierarchy used to discuss bonded NiO_2 intermediates.

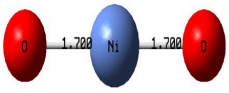
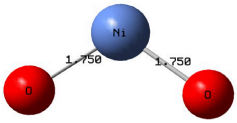
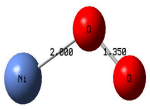
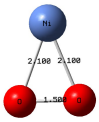
For clarity, the relative Gibbs free energies reported in Table 2 are referenced to the lowest-energy chemically bonded NiO_2 structure, namely the linear quintet O–Ni–O species. Consequently, the negative ΔG_{rel} values obtained for the non-bonded triplet Ni···O_2 solutions indicate that these arrangements lie below the bonded reference within the explored dataset. They should not be interpreted as members of the bonded NiO_2 hierarchy.

The unrestricted singlet calculations initiated from broken-symmetry guesses converged to final $\langle S^2 \rangle$ values of zero. Therefore, these results should not be interpreted as genuine broken-symmetry electronic states. Instead, the unrestricted wavefunctions collapsed to essentially closed-shell singlet solutions during the optimization procedure. For the linear, end-on, and side-on starting geometries, the restricted and BS-initialized unrestricted singlet calculations converged to equivalent structures and Gibbs free energies and were therefore treated as duplicated electronic solutions.

The angular starting geometry represents a particular case. The restricted singlet and the BS-initialized unrestricted singlet optimizations converged to two distinct angular local-minimum geometries, with rNi–O values of 1.584 and 1.566 Å and relative Gibbs

free energies of 83.12 and 60.97 kcal mol^{-1}, respectively. Because both calculations have final $\langle S^2 \rangle$ values of zero, the lower-energy angular structure is not assigned as a genuine broken-symmetry state. Instead, the two results are interpreted as distinct closed-shell angular local minima reached through different optimization pathways. The notation "BS-initialized" is retained only to document the initial wavefunction guess used in the corresponding calculation.

Table 2. Relative Gibbs free energies and optimized structural parameters of the NiO_2 species obtained from different initial geometries and electronic states. BS-initialized denotes an unrestricted singlet calculation initiated from a broken-symmetry guess. The symbol "—" indicates that the corresponding bond distance does not apply to the optimized structure. The $\langle S^2 \rangle$ values are reported as rounded integers.

Initial Geometry	Electronic State	Final Geometry	rNi–O (Å)	rO–O (Å)	ΔG_{rel} (kcal mol^{-1})	$\langle S^2 \rangle$
Linear 	Singlet	Linear	1.526	—	65.89	0
	Singlet BS	Linear	1.526	—	65.89	0
	Triplet	Linear	1.724	—	16.78	2
	Quintet	Linear	1.722	—	0.00	6
Angular 	Singlet	Angular	1.584	—	83.12	0
	Singlet BS	Angular	1.566	—	60.97	0
	Triplet	Linear	1.720	—	23.28	2
	Quintet	Linear	1.721	—	3.46	6
End-on 	Singlet	Side-on	1.779	1.370	22.76	0
	Singlet BS	Side-on	1.779	1.370	22.76	0
	Triplet	Dissociated Ni + O_2	—	1.322	−3.60	2
Side-on 	Singlet	Side-on	1.779	1.370	22.76	0
	Singlet BS	Side-on	1.779	1.370	22.77	0
	Triplet	Dissociated Ni + O_2	—	1.321	−3.57	2
	Quintet	Dissociated Ni + O_2	—	1.325	32.74	6

Note: The terms end-on and side-on describe the coordination mode of the O_2 moiety to the Ni atom. In the end-on configuration, O_2 coordinates to Ni through only one oxygen atom (η^1-O_2 coordination). In the side-on configuration, both oxygen atoms interact with Ni simultaneously (η^2-O_2 coordination). The term "dissociated Ni + O_2" indicates that the optimization results in the separation of the Ni atom from the O_2 fragment.

To avoid ambiguity, structures were classified as chemically bonded NiO_2 minima only when the optimized geometry retained at least one well-defined Ni–O connectivity within a chemically meaningful bonding range and when the structure was confirmed as a true minimum by the absence of imaginary vibrational frequencies. Optimized arrangements in which the nickel atom and the dioxygen fragment became spatially separated were classified as non-bonded Ni···O_2 solutions. These species are relevant to identifying the system's global energetic limit. Still, they do not represent bound oxygen-rich nickel intermediates and are therefore not discussed as members of the bonded NiO_2 hierarchy.

Within the subset of vibrationally stable bonded NiO_2 structures, the linear quintet O–Ni–O species was identified as the lowest-energy minimum. This structure was therefore adopted as the reference for comparing bonded monomeric intermediates, not as

the global minimum of the complete Ni + O_2 potential energy surface. The optimized geometry exhibits two nearly equivalent Ni–O bonds and no retained O–O bond, indicating a complete reorganization from a dioxygen adduct into a dioxo-like arrangement. This result suggests that, once a chemically bound NiO_2 framework is imposed, the system preferentially stabilizes a high-spin linear O–Ni–O motif rather than a side-on dioxygen complex.

The relaxation of the angular starting geometry provides additional evidence that the linear O–Ni–O arrangement is the preferred bonded motif within the explored monomeric subset. In the quintet state, the initially angular structure did not retain its original shape. Still, it converged toward a linear geometry with Ni–O distances close to those obtained from the linear starting point. This convergence of distinct initial geometries toward a single structural family indicates that the bonded NiO_2 potential-energy surface favors a high-spin, dioxo-like arrangement, provided the analysis is restricted to vibrationally stable, chemically bonded minima.

The corresponding triplet structures were also confirmed to be true minima, but were less stable than the quintet reference. Although the triplet linear forms display slightly shorter Ni–O distances, this bond contraction does not compensate for the electronic stabilization associated with the quintet state. Therefore, the energetic ordering cannot be rationalized solely from the Ni–O bond length; it also depends on the spin-state-dependent electronic structure of the Ni–O framework. This result supports the need to evaluate multiple multiplicities rather than assigning the ground state based on geometry alone.

The side-on η^2-O_2 motif constitutes the second relevant bonded structural class. Both end-on and side-on starting geometries converged to an equivalent singlet side-on minimum, characterized by two Ni–O interactions and a retained O–O bond. The optimized O–O distance is longer than expected for free molecular oxygen, consistent with activation of the coordinated dioxygen fragment. However, this side-on structure remains higher in energy than the linear quintet within the bonded subset, indicating that preservation of the O_2 fragment is not the most favorable stabilization mode for the isolated bonded monomer at the present level of theory.

Structurally, the comparison between the two bonded families distinguishes two different oxygen-binding regimes. The linear quintet no longer retains an O–O bond and is better described as a reorganized dioxo-like O–Ni–O species. In contrast, the singlet side-on form preserves a coordinated dioxygen motif, although with an elongated O–O bond indicative of activation. Thus, the side-on species can be interpreted as a metastable bonded monomer with partial dioxygen character, whereas the linear quintet represents the more stable reorganized bonded form.

Structures presenting imaginary vibrational frequencies were excluded from the final hierarchy of true minima. Unrestricted singlet calculations initiated from broken-symmetry guesses were examined separately. In all cases, the final $\langle S^2 \rangle$ values were zero, indicating collapse to essentially closed-shell singlet solutions. Therefore, these calculations were not interpreted as genuine broken-symmetry electronic states. When the restricted and BS-initialized unrestricted calculations converged to the same geometry and Gibbs free energy, they were treated as duplicated solutions. In the angular case, the two optimization pathways converged to distinct closed-shell angular local minima and were therefore retained as separate geometric solutions.

3.2. Electronic Differentiation Between Linear O–Ni–O and Side-On η^2-O_2 Motifs Using ELF and LOL Analysis

ELF and LOL analyses were used as complementary localization descriptors to compare the electronic organization of the two representative bonded NiO_2 motifs: the linear

O–Ni–O structure and the side-on η^2-O_2 adduct (Figure 1). These descriptors were not used to quantify charge transfer or electron-density accumulation, which would require electron-density difference maps or population analyses. Instead, they were employed to evaluate whether the optimized structures exhibit separated localization domains associated with terminal oxo-like centers or a more continuous localization pattern associated with a retained dioxygen fragment. This distinction is relevant because the linear structure and the side-on adduct differ not only in geometry but also in the distribution of oxygen-centered electron localization.

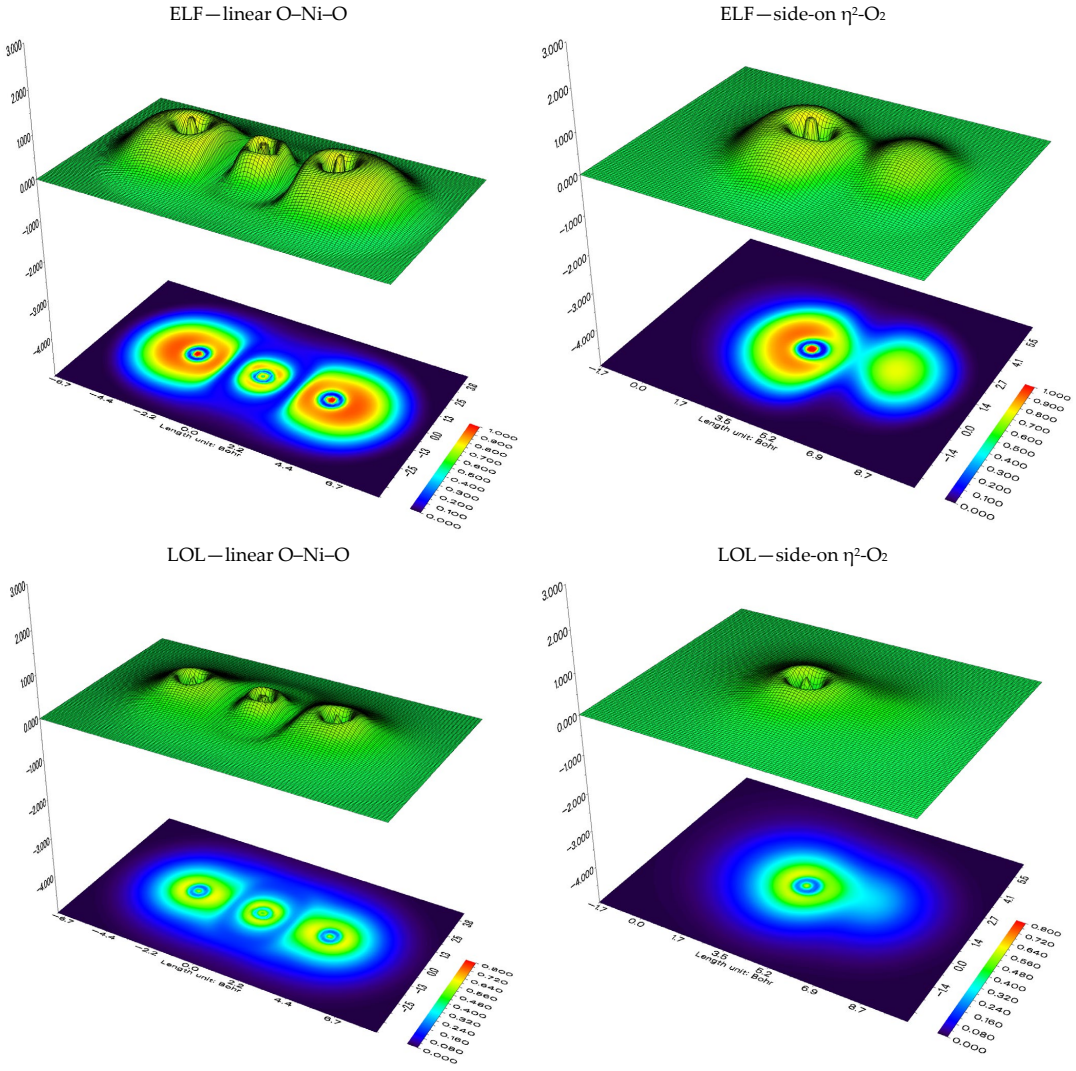


Figure 1. Two-dimensional ELF and LOL maps for NiO_2 linear O–Ni–O and side-on η^2-O_2 motifs.

In the linear O–Ni–O motif, the ELF map exhibits a clearly segmented, approximately symmetric distribution along the molecular axis. Three main localization domains are distinguished: two extensive regions associated with terminal oxygen atoms and a more contracted central region around nickel. This topology indicates that the electron density is spatially organized into well-defined and separate domains, with no evidence of a continuous accumulation between the two oxygens, which indicates the absence of persistent O–O bonding character. Consequently, the observed pattern is consistent with a completely rearranged dioxo species, in which nickel connects two equivalent oxygenated ends, but without retaining an identifiable dioxygenated fragment.

The LOL analysis of the same linear motif reinforces this interpretation. The surface also shows three well-defined localization maxima, with a clear separation between the

extreme regions and the central domain. In addition, the spatial similarity between the two basins associated with oxygen confirms the electronic equivalence of the two ends, in line with the practically identical Ni–O distances. Therefore, both ELF and LOL describe a highly symmetrical and compartmentalized electronic organization, compatible with a species in which the density has been redistributed toward two equivalent, well-defined Ni–O interactions. This behavior suggests a more electronically ordered state, in which structural reorganization has already eliminated the coordinated dioxygen character.

In contrast, the side-on species η^2-O_2 has a distinctly different electron topology. In the ELF map, the tripartite segmentation observed in the linear form disappears, and a more continuous, asymmetrical distribution emerges, dominated by a larger localization region near the coordinated oxygenated fragment. The density is not organized into two independent terminal oxygen domains but into a more coupled unit, indicating that the system retains part of the molecular character of the O_2 fragment. This behavior is consistent with the geometry of the side-on species, in which the O–O bond remains intact at a length of 1.370 Å, consistent with significant activation but not a complete break.

The LOL map confirms this same trend. Unlike the linear case, the distribution of localization in the side-on form is more diffuse and continuous, with a smoother transition between the region associated with nickel and the region corresponding to the coordinated O_2 fragment. This spatial continuity reveals a greater degree of electronic delocalization within the Ni–O_2 unit and suggests that the metal–dioxygen lateral interaction does not lead to the complete isolation of the two terminal oxygen centers. In other words, the electron density in side-on geometry still retains the imprint of a recognizable dioxygen fragment, albeit polarized and disturbed by coordination to the metallic center.

The comparison between the two species reveals a fundamental electronic difference. The linear O–Ni–O motif is characterized by a more defined, symmetrical, and segmented location, typical of a completely reorganized dioxo species. In contrast, the side-on form η^2-O_2 shows a less resolved and more continuous localization, compatible with a bonded state in which the O–O bond still participates directly in the electronic structure. From this perspective, the distinction between the two topologies is not only geometric, but also electronic: the linear species represents a state in which the density is redistributed towards two equivalent Ni–O bonds, while the side-on structure retains an organization closer to that of a metal–dioxygen complex.

Therefore, ELF and LOL support the structural assignment obtained from the optimized geometries. The linear O–Ni–O species exhibits a localization pattern compatible with two electronically distinct oxo-like regions connected by nickel. In contrast, the side-on η^2-O_2 structure retains a more coupled localization domain associated with the coordinated dioxygen fragment. This analysis should be interpreted qualitatively, as a descriptor of electron localization rather than as a direct measure of charge transfer. A more quantitative assessment of metal–oxygen charge redistribution would require additional descriptors such as spin-density maps, natural population analysis, bond orders, or electron-density difference plots.

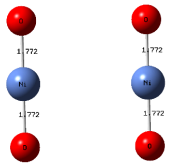
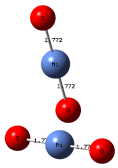
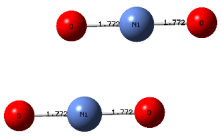
Because the investigated systems are finite molecular clusters rather than periodic solids, the concept of a bulk band gap is not directly applicable. A frontier-orbital analysis based on the HOMO–LUMO energy separation could provide complementary information about the electronic response of the optimized structures. However, such an analysis was not included in the present dataset and is therefore identified as a relevant direction for future work.

3.3. Structural and Thermodynamic Evolution of Aggregates $(NiO_2)_n$

The successive aggregation of NiO_2 units leads to a nontrivial structural evolution, in which both the preferred topology and the distribution of the Ni–O terminal and bridging links change. Overall, the results show that the system goes from favoring a relatively compact nucleus in the dimer to progressively more open architectures in the trimer and tetramer. This transition is reflected not only in the energy hierarchy of the optimized species but also in the aggregate, which retains terminal oxygens at the ends while increasing the number of Ni–O–Ni bridge interactions in the inner region.

For the dimer, the potential energy surface clearly favors the compact non-planar family. Within the set of linked species, the minimum corresponds to the compact non-planar quintet, with a free energy G of −3317.30 hartree and a relative free energy of 0.00 kcal mol^{-1}. Very close to this is the triplet of the same family, whose energy penalty is only 1.8963 kcal mol^{-1}. In contrast, the parallel open topology is significantly less stable, with a quintet located 24.07 kcal mol^{-1} above the minimum. At the same time, the semicyclic form has even lower energy competitiveness and, in the case of the quintet, vibrational instability. From the structural point of view, the most stable dimer corresponds to a closed species, linked by two bridging oxygens and topped by terminal oxygens at both ends. In this geometry, the terminal Ni–O links are between 1.765 and 1.783 Å, while the Ni–O bridge links are distributed between 1.919 and 1.944 Å. This differentiation is consistent with a structure in which the oxo ends retain a more localized character. At the same time, the bridging oxygens stabilize the metal core through somewhat longer and shared interactions (Table 3).

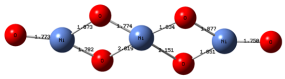
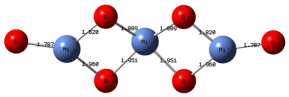
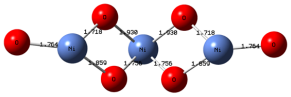
Table 3. Relative Gibbs free energies of the optimized $(NiO_2)_2$ dimer structures obtained from different initial geometries and electronic states.

Initial Geometry	Electronic State	Multiplicity	Final Geometry	ΔG_{rel} (kcal mol^{-1})
 Parallel open	Singlet	1	Cyclic $(\mu\text{-O})_2$-bridged dimer	108.22
	Triplet	3	Distorted cyclic $(\mu\text{-O})_2$-bridged dimer	46.84
	Quintet	5	Cyclic $(\mu\text{-O})_2$-bridged dimer	24.07
 Non-planar compact	Singlet	1	Compact O–O-containing bridged dimer	120.89
	Triplet	3	Cyclic $(\mu\text{-O})_2$-bridged dimer	1.90
	Quintet	5	Cyclic $(\mu\text{-O})_2$-bridged dimer	0.00
 Semi-cyclic	Singlet	1	Cyclic $(\mu\text{-O})_2$-bridged dimer	108.55
	Triplet	3	Distorted cyclic $(\mu\text{-O})_2$-bridged dimer	35.89
	Quintet	5	Separated Ni_2 units	47.03

Note: The notation μ-O indicates an oxygen atom that bridges the two Ni centers. The term "cyclic $(\mu\text{-O})_2$-bridged dimer" refers to a Ni_2O_2 core containing two bridging oxygen atoms and two terminal oxygen atoms. The term "distorted cyclic" denotes an analogous connectivity with non-equivalent Ni–O bond distances. The term "compact O–O-containing bridged dimer" describes the structure in which the central oxygen atoms remain in proximity and interact with both Ni centers. "Separated NiO_2 units" indicates that the optimization does not lead to a bound Ni_2O_4 dimer.

Upon increasing the aggregate size to $(NiO_2)_3$, the preferred topology changes dramatically. In this case, the global minimum of the explored set corresponds to the bridged open structure in multiplicity 5, with a free energy G of −4975.98 hartree and a relative free energy of 0.00 kcal mol^{-1}. The triplet and septet variants of this same family are located at 23.34 and 32.61 kcal mol^{-1}, respectively. In contrast, the compact non-planar and semicyclic curved families are displaced to a considerably less stable region, with energy differences in the order of 40 to 69 kcal mol^{-1}. This behavior indicates that, starting at $n = 3$, compaction ceases to be the dominant mode of stabilization, and the system begins to favor chain propagation of the metal-oxo frame. The most stable trimeric structure adopts an open chain of three Ni centers linked by successive oxygen bridges, with terminal oxygens preserved at both ends of the aggregate. The terminal Ni–O bonds remain within a narrow range, approximately 1.766–1.783 Å, very close to that observed for the dimer, while the Ni–O bridge bonds lie between 1.888 and 1.945 Å. This regularity suggests that aggregate growth occurs by incorporating new bridged units without substantially altering the nature of the terminal ends, although it does expand the internal skeleton. On the other hand, the compact, non-planar, and semicyclic curved forms show a greater dispersion of Ni–O bridge distances, with values close to 2.00 Å and even higher in some contacts, indicating less homogeneous connectivity and lower stabilizing efficiency (Table 4).

Table 4. Relative Gibbs free energies of the optimized $(NiO_2)_3$ trimer structures obtained from different initial geometries and electronic states.

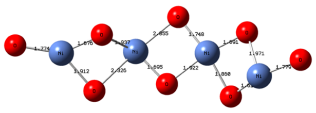
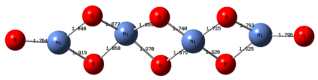
Initial Geometry	Electronic State	Multiplicity	Final Geometry	ΔG_{rel} (kcal mol^{-1})
 Bridged open	Triplet	3	Open μ-O-bridged chain	23.34
	Quintet	5	Open μ-O-bridged chain	0.00
	Septet	7	Open μ-O-bridged chain	32.61
 Non-planar compact	Triplet	3	Open μ-O-bridged chain	48.53
	Quintet	5	Open μ-O-bridged chain	41.92
	Septet	7	Open μ-O-bridged chain	68.98
 Semi-cyclic curved	Triplet	3	Open μ-O-bridged chain	48.17
	Quintet	5	Compact semi-cyclic μ-O-bridged structure	40.85
	Septet	7	Open μ-O-bridged chain	67.91

Note: The term "open μ-O-bridged chain" describes an extended Ni_3O_6 arrangement in which the Ni centers are connected through bridging oxygen atoms without forming a compact cyclic structure. The term "compact semi-cyclic μ-O-bridged structure" denotes a partially closed and distorted arrangement containing bridging oxygen atoms. These structural labels are descriptive and do not imply a formal assignment of the oxidation states or the oxo, peroxo, or superoxo character of the oxygen-containing fragments.

Taken together, the evolution of the $(NiO_2)_n$ aggregates suggests a size-dependent structural reorganization within the conformational space explored in this work. For the dimer, the lowest-energy bonded structure corresponds to a relatively compact bridged nucleus, stabilized by terminal Ni–O bonds and two internal Ni–O–Ni bridges. For the tetramer, the explored conformational space was more limited than for the smaller clusters; therefore, the conclusions must be interpreted with caution. Among the two optimized open-chain structures considered, the open curved arrangement in multiplicity 7 gives the lowest Gibbs free energy. It is therefore taken as the reference structure for the $(NiO_2)_4$ subset (Table 5). The pointed-open variant lies at a higher energy by approximately 25.6 kcal mol^{-1}. Both structures preserve an extended Ni–O framework with terminal oxygen

atoms and internal Ni–O–Ni bridges. Thus, within the currently explored tetrameric space, open high-spin architectures remain competitive; however, a more exhaustive search, including compact, cyclic, and additional high-spin alternatives, would be required before establishing a general size-dependent rule for larger $(NiO_2)_n$ clusters.

Table 5. Optimized structures, spin multiplicities, and relative Gibbs free energies of the tetrameric $(NiO_2)_4$ topologies.

Initial Geometry	Final Geometry	rNi–O (Term) (Å)	rNi–μ-O (Å)	Multiplicity	ΔG_{rel} (kcal/mol)
 Open curved	Open curved	≈1.76–1.78	1.685–1.987	7	0
 Pointed open	Pointed open	1.779–1.798	1.685–1.979	7	25.68

The bond-distance analysis supports this interpretation. Terminal Ni–O bonds remain comparatively conserved throughout the series, generally within the range of approximately 1.76–1.79 Å, suggesting that the chemical character of the terminal oxo-like sites is largely preserved during aggregation. In contrast, the Ni–O bridge distances constitute the main structural variable. In the most stable dimer, these bridge distances are concentrated around 1.92–1.94 Å; in the most stable trimer, they are distributed approximately between 1.89 and 1.95 Å; and in the corrected tetrameric reference structure, a broader dispersion is observed in the inner region, consistent with greater local differentiation of the bridge sites. From a thermodynamic perspective, this behavior indicates that aggregation is governed by a balance between terminal Ni–O stabilization, internal bridge relaxation, and spin-state preference, rather than by a simple monotonic increase in compactness.

Taken together, the optimized structures suggest that the preferred aggregation pattern changes with cluster size within the explored conformational space. The dimer favors a compact bridged motif, whereas the trimer and the currently evaluated tetrameric candidates favor more extended Ni–O frameworks. This trend should not be interpreted as a definitive rule for all $(NiO_2)_n$ clusters, because the number of possible isomers increases rapidly with n, and the present study does not constitute a global optimization for $n > 4$. Nevertheless, the results indicate that aggregation is not a simple addition of equivalent NiO_2 units. Instead, cluster growth involves a balance between terminal Ni–O stabilization, formation of internal Ni–O–Ni bridges, spin-state preference, and structural relaxation of the oxygen-rich framework.

3.4. O_2 Evolution and Cluster Reorganization

A preliminary O_2-release pathway was examined to evaluate whether an oxygen-rich tetrameric cluster can undergo molecular-oxygen evolution after internal structural reorganization. The profile was constructed from independently optimized stationary points corresponding to a selected tetrameric reference structure, a transition-state candidate, a reorganized intermediate, and a final configuration containing a detached O_2 molecule (Figure 2). The relative Gibbs free energies are referenced exclusively to the selected tetrameric reactant.

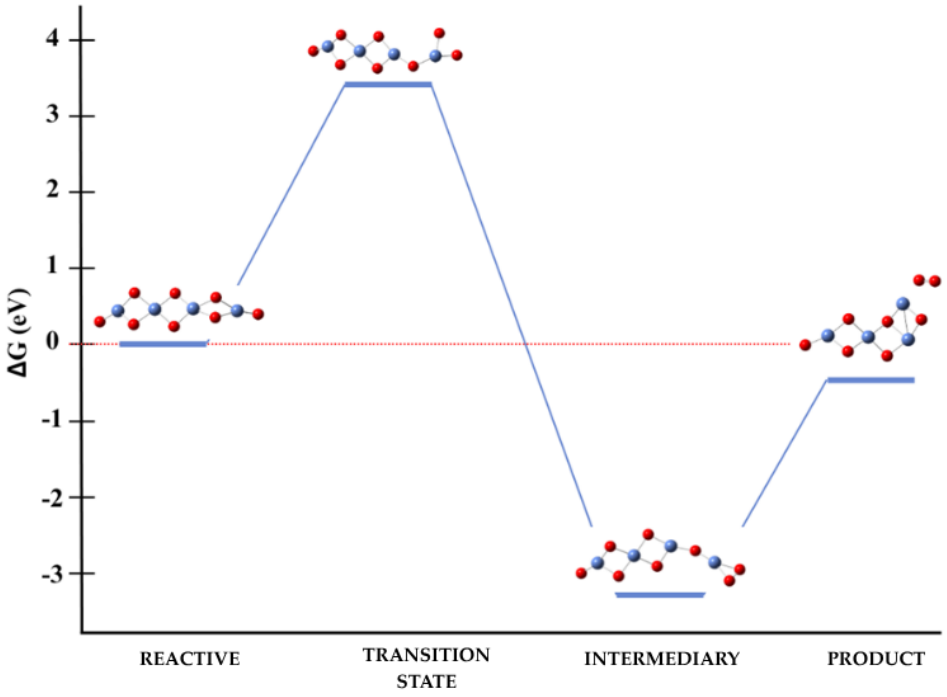


Figure 2. Proposed Gibbs free energy profile for the release of O_2 from the selected tetrameric structure $(NiO_2)_4$ with multiplicity 7. The profile includes the optimized tetrameric reactant, the transition-state candidate, the rearranged intermediate, and the final product containing the released O_2.

The proposed profile suggests that a simple dissociation event does not represent O_2 release. Instead, the explored sequence involves a substantial reorganization of the Ni–O framework prior to the separation of the dioxygen fragment. The transition-state candidate lies approximately 3.4 eV above the selected reference structure, indicating that the transformation is associated with a considerable energetic barrier within the explored pathway. After this barrier, the system reaches a reorganized intermediate located at a lower relative Gibbs free energy than the initial tetrameric reference structure.

The reorganized intermediate was characterized as a stationary point without any imaginary frequencies, whereas the transition-state candidate exhibited a single imaginary frequency along the expected reaction coordinate. However, the present analysis does not constitute an exhaustive search for reaction paths or a global optimization of the Ni_4O_8 potential-energy surface. Therefore, the reorganized structure should be interpreted as a relevant stationary point within the explored pathway rather than as definitive evidence of the global minimum of the tetrameric system.

The final configuration, consisting of a reorganized nickel–oxygen fragment and detached molecular oxygen, lies below the selected tetrameric reference structure. This result indicates that O_2 evolution may become thermodynamically accessible after substantial internal reorganization. Nevertheless, the proposed profile should be regarded as a preliminary mechanistic model. Additional conformational sampling and explicit analysis of possible spin-crossing pathways would be required to establish a complete kinetic mechanism.

4. Conclusions

The DFT analysis of small $(NiO_2)_n$ clusters with n = 1–4 shows that their structural and energetic behavior is strongly dependent on topology, spin multiplicity, and the distinction between bonded and non-bonded solutions. For the NiO_2 monomer, the lowest-energy structure of the completely explored set corresponds to a non-bonded Ni···O_2 arrangement.

However, within the subset of chemically bonded and vibrationally stable NiO_2 minima, the linear high-spin O–Ni–O structure is preferred over the side-on η^2-O_2 adduct. This indicates that preservation of a coordinated dioxygen fragment is not the most favorable stabilization mode for the bonded monomer; instead, the system tends to reorganize toward a dioxo-like structure.

For the aggregates, the results suggest a size-dependent change in preferred topology within the explicitly examined conformational space. The dimer favors a compact bridged arrangement, whereas the trimer and the evaluated tetrameric candidates favor more extended Ni–O frameworks. This behavior indicates that aggregation involves progressive reorganization of terminal Ni–O bonds and internal Ni–O–Ni bridges, rather than a simple addition of equivalent NiO_2 units. However, because the number of possible isomers increases rapidly with cluster size, these trends should not be extrapolated to larger $(NiO_2)_n$ systems without additional conformational sampling.

The preliminary O_2-release profile indicates that molecular-oxygen evolution from the selected tetrameric structure is associated with a substantial reorganization of the Ni–O framework. The explored stationary-point sequence supports the interpretation of small $(NiO_2)_n$ clusters as metastable, oxygen-rich intermediates rather than as species that necessarily dissociate immediately. However, the tetrameric profile should be interpreted as an exploratory mechanistic model within the evaluated structural and spin-state space. A complete description of the reaction landscape would require broader conformational sampling and explicit evaluation of possible spin-crossing pathways.

Supplementary Materials: The following supporting information can be downloaded at: https://www.mdpi.com/article/10.3390/chemistry8070087/s1. Table S1. Coordinates for linear NiO_2 with singlet, singlet (broken symmetry), triplet, and quintet multiplicities; Table S2. Coordinates for angular NiO_2 with singlet, singlet (broken symmetry), triplet, and quintet multiplicities; Table S3. Coordinates of the NiO_2 molecule in the end-on orientation with singlet, singlet (broken symmetry), triplet, and quintet multiplicities; Table S4. Coordinates of the NiO_2 molecule in the side-on orientation with singlet, singlet (broken symmetry), triplet, and quintet multiplicities; Table S5. Coordinates of the $(NiO_2)_2$ molecule in the "Parallel Open" configuration with singlet, triplet, and quintet multiplicities; Table S6. Coordinates of the $(NiO_2)_2$ molecule in the "non-planar compact" configuration with singlet, triplet, and quintet multiplicities; Table S7. Coordinates of the $(NiO_2)_2$ molecule in the "Semi-cyclic" configuration with singlet, triplet, and quintet multiplicities; Table S8. Coordinates of the $(NiO_2)_3$ molecule in the "Bridged open" configuration with triplet, quintet and septet multiplicities; Table S9. Coordinates of the $(NiO_2)_3$ molecule in the "Non-planar compact" configuration with triplet, quintet and septet multiplicities; Table S10. Coordinates of the $(NiO_2)_3$ molecule in the "Semi-cyclic curved" configuration with triplet, quintet and septet multiplicities; Table S11. Coordinates of the $(NiO_2)_4$ molecule in the "Open curved" configuration with septet multiplicities; Table S12. Coordinates of the $(NiO_2)_4$ molecule in the "Pointed open" configuration with septet multiplicities; Figure S1. Initial and final geometries, multiplicities, relative free energies, and vibrational stability of the monomer topologies were evaluated for NiO_2; Figure S2. Initial and final geometries, multiplicities, relative free energies, and vibrational stability of the dimeric topologies were evaluated for $(NiO_2)_2$; Figure S3. Initial and final geometries, multiplicities, relative free energies, and vibrational stability of the trimeric topologies were evaluated for $(NiO_2)_3$; Figure S4. Initial and final geometries, multiplicities, and relative free energies of the tetrameric topologies evaluated for $(NiO_2)_4$.

Author Contributions: Conceptualization, J.H.-F., R.G.-C. and R.O.-T.; Methodology, J.H.-F.; Software, J.H.-F.; Validation, J.H.-F.; Formal analysis, J.H.-F., R.G.-C. and R.O.-T.; Investigation, J.H.-F., R.G.-C. and R.O.-T.; Resources, J.H.-F.; Data curation, J.H.-F.; Writing—original draft, J.H.-F. and R.O.-T.; Writing—review & editing, J.H.-F., R.G.-C. and R.O.-T.; Visualization, J.H.-F., R.G.-C. and R.O.-T.;

Supervision, J.H.-F.; Project administration, J.H.-F.; Funding acquisition, J.H.-F. All authors have read and agreed to the published version of the manuscript.

Funding: This research received no external funding.

Data Availability Statement: The original contributions presented in this study are included in the article/Supplementary Material. Further inquiries can be directed to the corresponding author.

Conflicts of Interest: The authors declare no conflicts of interest.

References

1. Hardwick, L.J.; De León, C.P. Rechargeable Multi-Valent Metal-Air batteries. *Johns. Matthey Technol. Rev.* **2018**, *62*, 134–149. [CrossRef]
2. Wang, H.-F.; Xu, Q. Materials design for rechargeable Metal-Air batteries. *Matter* **2019**, *1*, 565–595. [CrossRef]
3. Chen, X.; Zhou, Z.; Karahan, H.E.; Shao, Q.; Wei, L.; Chen, Y. Recent advances in materials and design of electrochemically rechargeable Zinc–Air batteries. *Small* **2018**, *14*, e1801929. [CrossRef] [PubMed]
4. Olabi, A.G.; Sayed, E.T.; Wilberforce, T.; Jamal, A.; Alami, A.H.; Elsaid, K.; Rahman, S.M.A.; Shah, S.K.; Abdelkareem, M.A. Metal-Air Batteries—A review. *Energies* **2021**, *14*, 7373. [CrossRef]
5. Wang, Q.; Kaushik, S.; Xiao, X.; Xu, Q. Sustainable zinc–air battery chemistry: Advances, challenges and prospects. *Chem. Soc. Rev.* **2023**, *52*, 6139–6190. [CrossRef] [PubMed]
6. Nazir, G.; Rehman, A.; Lee, J.-H.; Kim, C.-H.; Gautam, J.; Heo, K.; Hussain, S.; Ikram, M.; AlObaid, A.A.; Lee, S.-Y.; et al. A review of Rechargeable Zinc–Air Batteries: Recent progress and future Perspectives. *Nano-Micro Lett.* **2024**, *16*, 138. [CrossRef] [PubMed]
7. Xing, P.; Sanglier, P.; Zhang, X.; Li, J.; Li, Y.; Su, B.-L. Advances in cathode materials for Li-O_2 batteries. *J. Energy Chem.* **2024**, *95*, 126–167. [CrossRef]
8. Ko, Y.; Kim, K.; Yoo, J.; Kwon, G.; Park, H.; Kim, J.; Lee, B.; Song, J.-H.; Kim, J.; Kang, K. Redox mediators for oxygen reduction reactions in lithium–oxygen batteries: Governing kinetics and its implications. *Energy Environ. Sci.* **2023**, *16*, 5525–5533. [CrossRef]
9. Gao, Z.; Temprano, I.; Lei, J.; Tang, L.; Li, J.; Grey, C.P.; Liu, T. Recent progress in developing a LIOH-Based reversible nonaqueous Lithium–Air battery. *Adv. Mater.* **2022**, *35*, e2201384. [CrossRef] [PubMed]
10. Song, J.; Wei, C.; Huang, Z.F.; Liu, C.; Zeng, L.; Wang, X.; Xu, Z.J. A review on fundamentals for designing oxygen evolution electrocatalysts. *Chem. Soc. Rev.* **2020**, *49*, 2196–2214. [CrossRef] [PubMed]
11. Lee, S.; Chu, Y.-C.; Bai, L.; Chen, H.M.; Hu, X. Operando identification of a side-on nickel superoxide intermediate and the mechanism of oxygen evolution on nickel oxyhydroxide. *Chem Catal.* **2022**, *3*, 100475. [CrossRef]
12. De Lara-Castells, M.P. First-principles modeling of the new generation of subnanometric metal clusters: Recent case studies. *J. Colloid Interface Sci.* **2022**, *612*, 737–759. [CrossRef] [PubMed]
13. Garcia, J.M.; Sayres, S.G. Orbital-dependent photodynamics of strongly correlated nickel oxide clusters. *Phys. Chem. Chem. Phys.* **2022**, *24*, 5590–5597. [CrossRef] [PubMed]
14. Kwon, S.; Deshlahra, P.; Iglesia, E. Reactivity and selectivity descriptors of dioxygen activation routes on metal oxides. *J. Catal.* **2019**, *377*, 692–710. [CrossRef]
15. Khazanov, T.M.; Mukherjee, A. Harnessing oxidizing potential of nickel for sustainable hydrocarbon functionalization. *Molecules* **2024**, *29*, 5188. [CrossRef] [PubMed]
16. McNeece, A.J.; Jesse, K.A.; Xie, J.; Filatov, A.S.; Anderson, J.S. Generation and oxidative reactivity of a NI(II) superoxo complex via Ligand-Based redox Non-Innocence. *J. Am. Chem. Soc.* **2023**, *142*, 10824–10832. [CrossRef]
17. Jeong, D.; Valentine, J.S.; Cho, J. Bio-inspired mononuclear nonheme metal peroxo complexes: Synthesis, structures and mechanistic studies toward understanding enzymatic reactions. *Coord. Chem. Rev.* **2023**, *480*, 215021. [CrossRef]
18. Cipriano, L.A.; Di Liberto, G.; Pacchioni, G. Superoxo and peroxo complexes on Single-Atom Catalysts: Impact on the oxygen evolution reaction. *ACS Catal.* **2022**, *12*, 11682–11691. [CrossRef]
19. Lee, H.S.; Shin, H.; Park, S.; Kim, J.; Jung, E.; Hwang, W.; Lee, B.-H.; Yoo, J.M.; Antink, W.H.; Lee, K.; et al. Electrochemically generated electrophilic peroxo species accelerates alkaline oxygen evolution reaction. *Joule* **2023**, *7*, 1902–1919. [CrossRef]
20. Yang, Y.; Li, J.; Li, C.; Gong, M.; Wang, X.; Yang, X.; Wang, H.; Li, Y.-F.; Liu, Z.-P. The identity of nickel peroxide as a nickel superoxyhydroxide for enhanced electrocatalysis. *JACS Au* **2023**, *3*, 2964–2972. [CrossRef] [PubMed]
21. Ramakrishnan, S.; Anjukandi, P. Superoxide to peroxide interconversion in Ni-TMC complexes: The significance of structure and spin states. *Inorg. Chem.* **2024**, *63*, 15186–15196. [CrossRef] [PubMed]
22. Butera, V. Density functional theory methods applied to homogeneous and heterogeneous catalysis: A short review and a practical user guide. *Phys. Chem. Chem. Phys.* **2024**, *26*, 7950–7970. [CrossRef] [PubMed]
23. Hales, N.; Schmidt, T.J.; Fabbri, E. Reversible and irreversible transformations of Ni-based electrocatalysts during the oxygen evolution reaction. *Curr. Opin. Electrochem.* **2023**, *38*, 101231. [CrossRef]

24. Lillo, H.L.; Buss, J.A. A dinuclear nickel peroxycarbonate complex: CO_2 addition promotes H_2O_2 release. *Chem. Commun.* **2024**, *60*, 8549–8552. [CrossRef] [PubMed]
25. De Amorim, R.V.; Batista, K.E.A.; Nagurniak, G.R.; Orenha, R.P.; Parreira, R.L.T.; Piotrowski, M.J. CO, NO, and SO adsorption on Ni nanoclusters: A DFT investigation. *Dalton Trans.* **2020**, *49*, 6407–6417. [CrossRef] [PubMed]
26. Imaoka, T.; Kuzume, A.; Tanabe, M.; Tsukamoto, T.; Kambe, T.; Yamamoto, K. Atom hybridization of metallic elements: Emergence of subnano metallurgy for the post-nanotechnology. *Coord. Chem. Rev.* **2022**, *474*, 214826. [CrossRef]
27. Granja-DelRío, A.; Abdulhussein, H.A.; Johnston, R.L. DFT-Based Global Optimization of Sub-nanometer NI–PD clusters. *J. Phys. Chem. C* **2019**, *123*, 26583–26596. [CrossRef]
28. Weigend, F.; Ahlrichs, R. Balanced basis sets of split valence, triple zeta valence and quadruple zeta valence quality for H to Rn: Design and assessment of accuracy. *Phys. Chem. Chem. Phys.* **2005**, *7*, 3297. [CrossRef] [PubMed]
29. Fernández, J.H.; Palomo, J.P.; Ortega-Toro, R. Application of DFT and Experimental Tests for the Study of Compost Formation Between Chitosan-1,3-dichloroketone with Uses for the Removal of Heavy Metals in Wastewater. *J. Compos. Sci.* **2025**, *9*, 91. [CrossRef]
30. Lehtola, S.; Marques, M.A.L. Many recent density functionals are numerically ill-behaved. *J. Chem. Phys.* **2022**, *157*, 174114. [CrossRef] [PubMed]
31. Bowling, P.E.; Dasgupta, S.; Herbert, J.M. Eliminating imaginary vibrational frequencies in Quantum-Chemical cluster models of enzymatic active sites. *J. Chem. Inf. Model.* **2024**, *64*, 3912–3922. [CrossRef] [PubMed]
32. Hanaway, D.J.; Kennedy, C.R. Automated Variable Electric-Field DFT application for evaluation of optimally oriented electric fields on chemical reactivity. *J. Org. Chem.* **2022**, *88*, 106–115. [CrossRef] [PubMed]
33. Reimann, M.; Kaupp, M. Spin-State splittings in 3D Transition-Metal Complexes Revisited: Toward a Reliable theory benchmark. *J. Chem. Theory Comput.* **2022**, *19*, 97–108. [CrossRef] [PubMed]
34. Xie, Y.; Liu, N.; Li, X.; Qin, X.; Luo, X.; Wang, Y.; Chen, X. The influence of Single-Atom $Fe^{2+/3+}N_4$ spin state on the electroreduction of CO_2 to CO/HCOOH by analyzing Proton/Electron transfer mechanisms and free energy evolutions. *J. Phys. Chem. C* **2021**, *125*, 21460–21470. [CrossRef]
35. Xu, H.; Zhu, J.Z.; Zou, C.; Zhang, F.; Ming, D.; Guan, D.; Ma, L. Theoretical design of Core–Shell 3D-Metal nanoclusters for efficient Hydrogen-Evolving reaction. *Energy Fuels* **2023**, *37*, 16781–16789. [CrossRef]
36. Badawy, S.A.; Abdel-Latif, E.; Mohamed, W.H.; Elmorsy, M.R. Unleashing synergistic co-sensitization of BOA dyes and Ru(ii) complexes for dye-sensitized solar cells: Achieving remarkable efficiency exceeding 10% through comprehensive characterization, advanced modeling, and performance analysis. *RSC Adv.* **2024**, *14*, 25549–25560. [CrossRef] [PubMed]
37. Silvi, B.; Savin, A. Classification of chemical bonds based on topological analysis of electron localization functions. *Nature* **1994**, *371*, 683–686. [CrossRef]
38. Schmider, H.L.; Becke, A.D. Chemical content of the kinetic energy density. *J. Mol. Struct. THEOCHEM* **2000**, *527*, 51–61. [CrossRef]
39. Malykhin, R.S.; Sukhorukov, A.Y. Electrophilic intermediates in the NEF and Meyer reactions: A computational study. *J. Org. Chem.* **2024**, *89*, 18109–18121. [CrossRef] [PubMed]

Disclaimer/Publisher's Note: The statements, opinions and data contained in all publications are solely those of the individual author(s) and contributor(s) and not of MDPI and/or the editor(s). MDPI and/or the editor(s) disclaim responsibility for any injury to people or property resulting from any ideas, methods, instructions or products referred to in the content.